EPJ Photovoltaics **14**, 8 (2023)

https://doi.org/10.1051/epjpv/2022034

Special Issue on 'WCPEC-8: State of the Art and Developments in Photovoltaics', edited by Alessandra Scognamiglio, Robert Kenny, Shuzi Hayase and Arno Smets

Available online at: www.epj-pv.org

REGULAR ARTICLE

OPEN ACCESS

Model for contact formation of novel TeO_2 containing Pb-free silver paste on n^+ and p^+ doped crystalline silicon

Fabian Geml[1,*], Benjamin Gapp[1], Simon Johnson[2,a], Patricia Sutton[2], Angela Goode[2], Jonathan Booth[2], Heiko Plagwitz[1] and Giso Hahn[1]

[1] University of Konstanz, Department of Physics, 78457 Konstanz, Germany
[2] Johnson Matthey Technology Centre, Sonning Common, Reading, RG4 9NH, UK

Received: 1 July 2022 / Received in final form: 8 October 2022 / Accepted: 16 December 2022

Abstract. Silver (Ag) pastes are widely used in the global market for most solar cell architectures. Thereby, lead (Pb) is no longer wanted in productions for environmental reasons. In this work, a model for the contact formation between Pb-free, tellurium oxide (TeO_2) containing screen-printable Ag pastes and silicon is presented. It is shown that Te plays a key role in this model. Te is not only an important part in etching the surface passivation layers with TeO_2 dissolving the dielectric layer but also for a formation of the contacts with Te forming a compound consisting of Ag_2Te. Using EDX mapping, local contact regions can be examined and interpreted for contact formation. The used paste system enables far more flexible paste mixturing leading to a novel developed commercial paste which is on a par with other pastes used in industry concerning the resulting contact properties. This is also demonstrated in this work by the very low contact resistivity of less than 1 $m\Omega cm^2$ over a wide range of firing peak temperatures. It is additionally shown that good resistivities can be achieved on both n^+- and p^+-doped regions.

Keywords: Metallization / silver / tellurium

1 Introduction

The global photovoltaic market is dominated by crystalline silicon (Si) wafer-based solar cells [1–4]. Although the industry will continue to rely on p-type wafers as the base material in the near future, there are manufacturers already today that are moving to n-type wafer-based concepts [5]. Regardless of which base material is used, most solar cells use an emitter of the other polarity on the front side covered by a passivation and antireflection layer [6,7]. For industrially manufactured electrodes, different metal pastes are deposited by screen printing. Traditionally, silver (Ag) was used in a fine-line finger grid for contacting n^+-type doped areas whereas aluminum (Al) over the entire surface for contacting p-type areas [8,9]. In the case of n-type base wafers where the p^+-type emitter is located on the front side, Ag or AgAl pastes have been used [10,11]. It is also possible to contact both sides and polarities with Ag paste, which in the case of application as a fine line grid on the rear offers the possibility of a bifacial solar cell architecture [12,13].

To enable the metal paste, regardless of its composition, to form an electrical contact to Si, normally a firing step is required, which is generally performed under ambient atmosphere and a peak temperature of up to 800 °C in a belt furnace [14,15]. During this firing step, the passivation layer, which can consist of silicon oxide (SiO_x), hydrogen-rich silicon nitride (SiN_x:H), aluminum oxide (AlO_x), or a combination thereof, must first be etched [16–18]. Recent studies explain the etching mechanism with the etching reaction of the glass frit normally included in the metal paste, which supports Ag crystal formation via a redox reaction [19–22]. It is reported that most likely Si and SiN_x:H are etched by the metal oxides [23–26]. In the classical view, lead oxide (PbO) was often identified here, but due to the general regulations on Pb and other environmental reasons, PbO is nowadays used less and less [27]. Another possibility for the etching reaction is assumed to be Ag_2O and oxidized Ag ions coming directly from the paste bulk [28–30]. These etch into the silicon material and are reduced there by existing charge carriers, forming silver crystallites on the wafer surface.

Since the global Ag paste market is moving from the former standard of PbO-based paste systems towards Pb-free formulations [31], e.g., Bi_2O_3/TeO_2-based systems, it is essential to understand how metals such as Bi, Te, and Zn affect metal/semiconductor contact formation in order

* e-mail: fabian.geml@uni-konstanz.de
[a] Now with Fenzi AGT Netherlands BV, 6222 NZ Maastricht, The Netherlands.

to optimize paste formulations. In this work, we present results leading to a new model that highlights Te as playing a key role for the Ag/Si contact formation.

2 Experimental

In this work, a novel metallization solution in which the conductive Ag paste does not contain glass particles is used. The system was reported for the first time in [32]. This technology consists of a Pb-free mixture of crystalline metal compounds, including the oxides of Te, Bi, Zn, Li and Na, milled and used as substitute flux for the typically used glass powders. In particular, the metal oxide mixture used does not contain silicon oxide.

The use of a simple mixture of finely milled crystalline metal compounds, rather than a glass frit, has several advantages. These include no glass frit forming step for paste manufacture and thus lower energy demand, being more environmentally friendly, lower production costs and complexity on the one hand. On the other hand, this furthers the potential for more flexibility in component mixtures, improving performance and flexibility for developing new recipes tailored for new solar cell designs.

During sample preparation, the monocrystalline n/p-type Czochralski (Cz)-grown Si substrates (4–5 Ωcm) were etched and cleaned. Samples were textured using a KOH-based alkaline solution with alcohol-based additives resulting in a random pyramid structure. Emitters were formed within a diffusion step in classic $POCl_3$ or BBr_3 tube furnace diffusions, respectively, forming an emitter sheet resistance of 85 Ω/sq with a peak concentration of $\approx 8 \times 10^{19}$ cm^{-3} for n^+ and 80 Ω/sq with a peak concentration of $\approx 7 \times 10^{19}$ cm^{-3} for p^+ (if not otherwise stated). Afterwards, the samples were etched in diluted HF and then coated with SiN_x:H via PECVD (plasma-enhanced chemical vapor deposition) for surface passivation. In a subsequent step, all samples were screen-printed with the developed Ag pastes in TLM (transfer length method) and grid structures. Then the samples were divided into two groups. One group was fired using a rapid thermal processing (RTP) furnace to provide more control in the range of low firing peak temperatures. The other sample group was (co-)fired in a standard solar cell belt furnace at various peak temperatures.

Several paste formulations have been tested. The paste finally used for solar cell-like samples in this study was substantially glass-free and comprised 1–3 wt.% of a crystalline metal oxide mixture; 88–90 wt.% of one or more metallic Ag powders and 9 wt.% of an organic vehicle. When not explicitly stated otherwise, this paste was used. Furthermore, additional pastes were used in investigating the reactions by varying the silver to mixed oxide (MO) ratio Ag:MO from 50%:50% to 75%:25% up to a complete system of MO (0%:100%).

The samples were first analyzed by applying TLM measurements and afterwards investigated by SEM (scanning electron microscopy)/TEM (transmission electron microscopy). Differences in material and composition can be observed via the contrast of the backscattered images, as the backscattered intensity is material specific. This was used to visualize the cross sections between the pure glass systems in their substrate. For TEM, small lamellas were cut by FIB (focused ion beam) and analyzed by mapped EDX (energy dispersive X-ray spectroscopy). EDX allows to obtain additional information about the atomic composition. Over a certain depth, the element characteristic X-rays can be analyzed to obtain information about a relative atomic density via the intensity. This was used to obtain information about the position and composition of the respective elements in the fired samples. XRD (X-ray diffraction) was also applied on some samples.

XRD can be used to investigate specific structures, bond configurations and pure element regions present at the analyzed spot. This allows certain compositions and crystalline formations (such as Bi_2TeO_5) to be identified without doubt in the following chapter.

3 Results and discussion

3.1 Paste potential

The behavior of the low temperature glassy phase formation of a paste containing a crystalline metal oxide mixture is different to that observed when using a paste containing a glass mixture made from the same composition of the crystalline metal oxides mixture. This is clearly observed in Figure 1 where the mixed crystalline oxides (left side) and a system with glass frits (right side) are compared. The upper section shows how the systems look in cross section taken using SEM when fired at a peak temperature of 250 °C using the RTP furnace. At temperatures of 250 °C and below (upper section in Fig. 1) the mixed oxide components have not yet reacted together and an inhomogeneous mix of crystalline raw materials is observed (as indicated by the changes in contrast for the backscatter SEM image). In comparison, the pre-formed glass material is homogeneous in composition. Please note that only a mix of oxides is used here and no silver has been added yet, which allows to compare the two systems on a fundamental level.

Systems fired at a peak temperature of 300 °C are shown in the bottom graphs of Figure 1. It can be seen that above the melting point of the oxides, which must therefore be between 250 °C and 300 °C, both systems behave similarly. For both systems, a merging of the structures can be observed with a simultaneous formation of bubbles due to the decomposition of the organics. This is an important point, as it shows that there is no reason why the considerations based on the system with mixed crystalline oxides should not also apply to those with glass frits.

Also indispensable for comparability at solar cell level is the consideration of the electrical properties of the contacts. It is clearly shown that the Ag paste is capable of simultaneously contacting both polarities very well ($POCl_3$ formed n^+-emitter and BBr_3 formed p^+-emitter) in Figure 2. One can observe the specific contact resistivity as a function of peak firing temperature for the sample group fired in the belt furnace. Values below 1 mΩcm^2 are achieved for a wide temperature window for these samples passivated with SiN_x:H. Efficiencies of >22.5% were reached at an industry partner's solar cell production line with this paste, proving the industrial applicability.

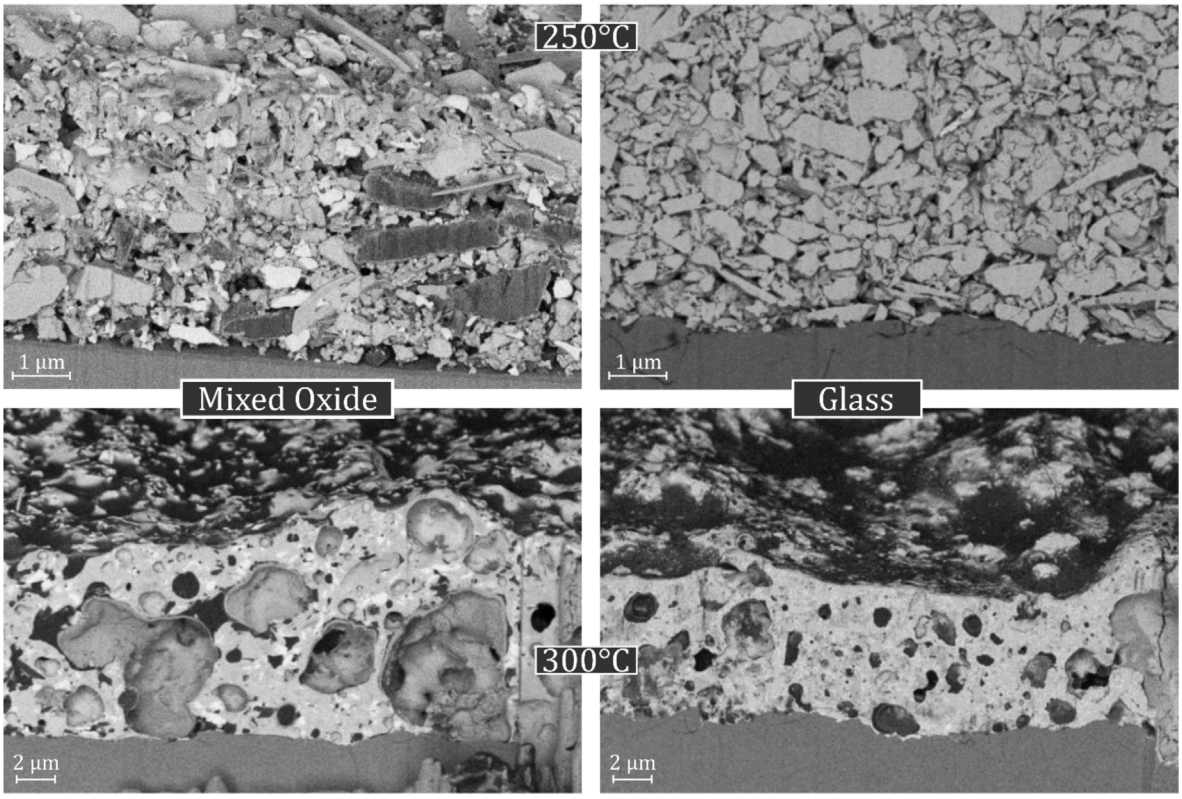

Fig. 1. SEM cross section pictures of pastes containing mixed crystalline oxides (left) and glass frits (right) fired with an RTP furnace at 250 °C (top) and 300 °C (bottom) show the difference between the two paste systems before and after melting of the oxides. Above the melting point, obviously between 250 °C and 300 °C, the paste bulks behave in a similar way.

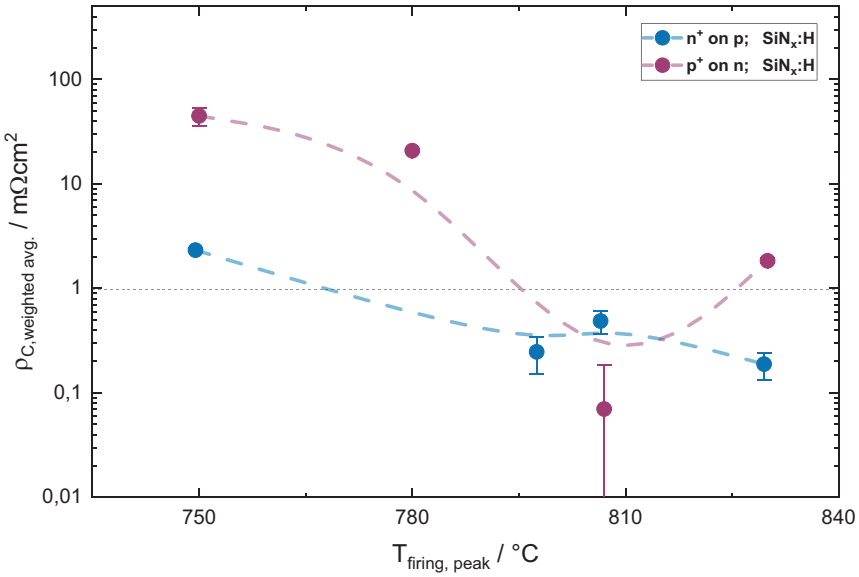

Fig. 2. Contact resistivity depending on sample peak firing temperature for the same Ag paste on different emitter types passivated with SiN_x:H. For both polarities, contact resistivities below 1 mΩcm^2 could be reached. Lines serve as a guide to the eye only.

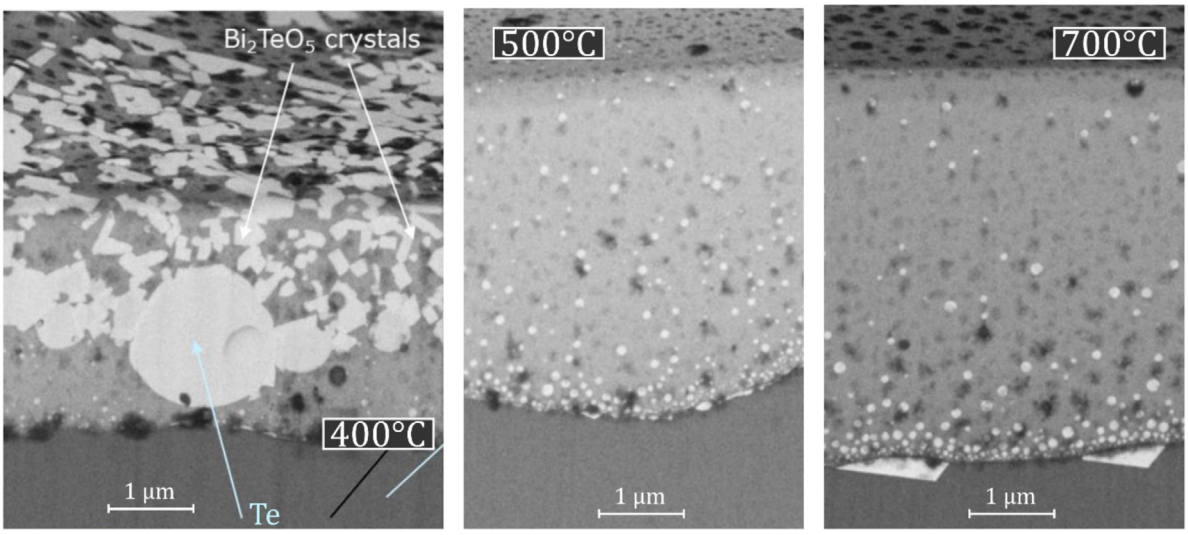

Fig. 3. SEM cross section images of a non-passivated sample for different RTP peak firing temperatures (400 °C left, 500 °C middle, 700 °C right). At 400 °C, there are large Te crystallites (bright blue arrow) as well as smaller Bi_2TeO_5 crystals (white arrows) visible, whereas the crystallization diminishes for higher peak temperatures. For 700 °C Te crystallites grown into the Si wafer are visible.

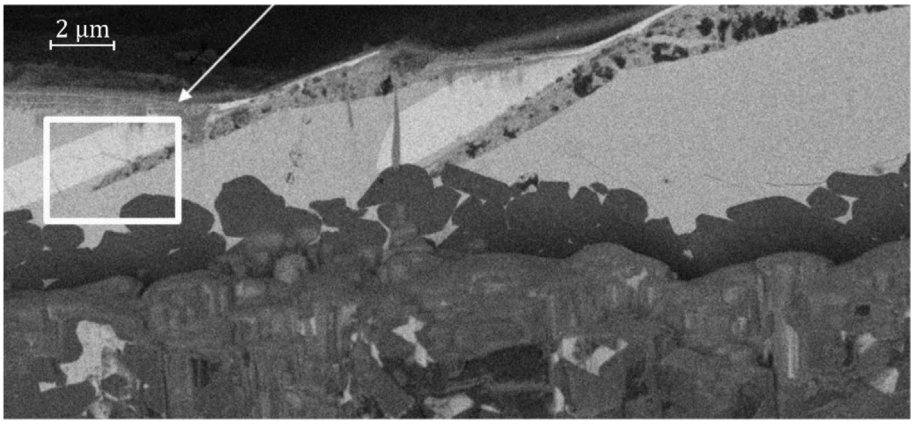

Fig. 4. SEM cross section picture of the same paste as before but on an alumina substrate, RTP fired at a peak temperature of 700 °C. No Te formation is visible, but large Bi-rich crystals, marked by the white rectangle and arrow.

3.2 Te movement

Formation of large Te-rich particles and additional crystalline phases can be observed in Figure 3 in the left SEM image when using the crystalline system. In addition to the crystallization of Bi_2TeO_5 [33,34] from the glassy phase, large Te crystals form here at the peak temperature of 400 °C due to reaction between the TeO_2 and the Si wafer.

The effect of an even higher increase in firing temperature is also investigated here, again followed by analysis via SEM imaging. Such an increase to 500 °C shows (Fig. 3, middle) that crystallization diminishes and SiO_2 begins to move into the glass matrix. Small Te particles are formed at the interface and move upward through the glass layer. A further increase up to 700 °C, as seen in Figure 3 on the right side, shows a further decrease in crystallization, but also Bi/Te spike-like growth into the wafer due to a redox reaction.

The Bi and Te spiking and adhesion onto a substrate surface is chemically dependent on a reduction or redox reaction of the Bi and Te glassy phases. Figure 4 shows the same paste as shown before, but belt furnace fired (peak temperature 700 °C) on an alumina substrate. Here, large Bi_2TeO_5 crystals are crystallized from the glassy phase, but no Bi or Te crystallites can be seen as before at the substrate surface. Since there is no redox reaction of Te and Bi with the Al_2O_3, no bismuth telluride phases or elemental Te can be formed. This is a key point in the reaction, since the elements in the paste need a partner with which a redox reaction is possible, such as silicon, for the reaction to continue as shown on Si substrate.

Additionally, there are important points regarding the further movement of the paste components after the redox reaction with silicon. In order to make this visible, the pastes are heavily interspersed with mixed crystalline oxides. Due to an Ag:MO ratio up to 50%:50%, the movement can be clearly observed. This can be obtained from the EDX maps in Figure 5. Please note that the magnification between the single pictures varies. On the left side the ratio of 50%:50% is depicted, on the right side of 75%:25%. From top to bottom increasingly higher RTP

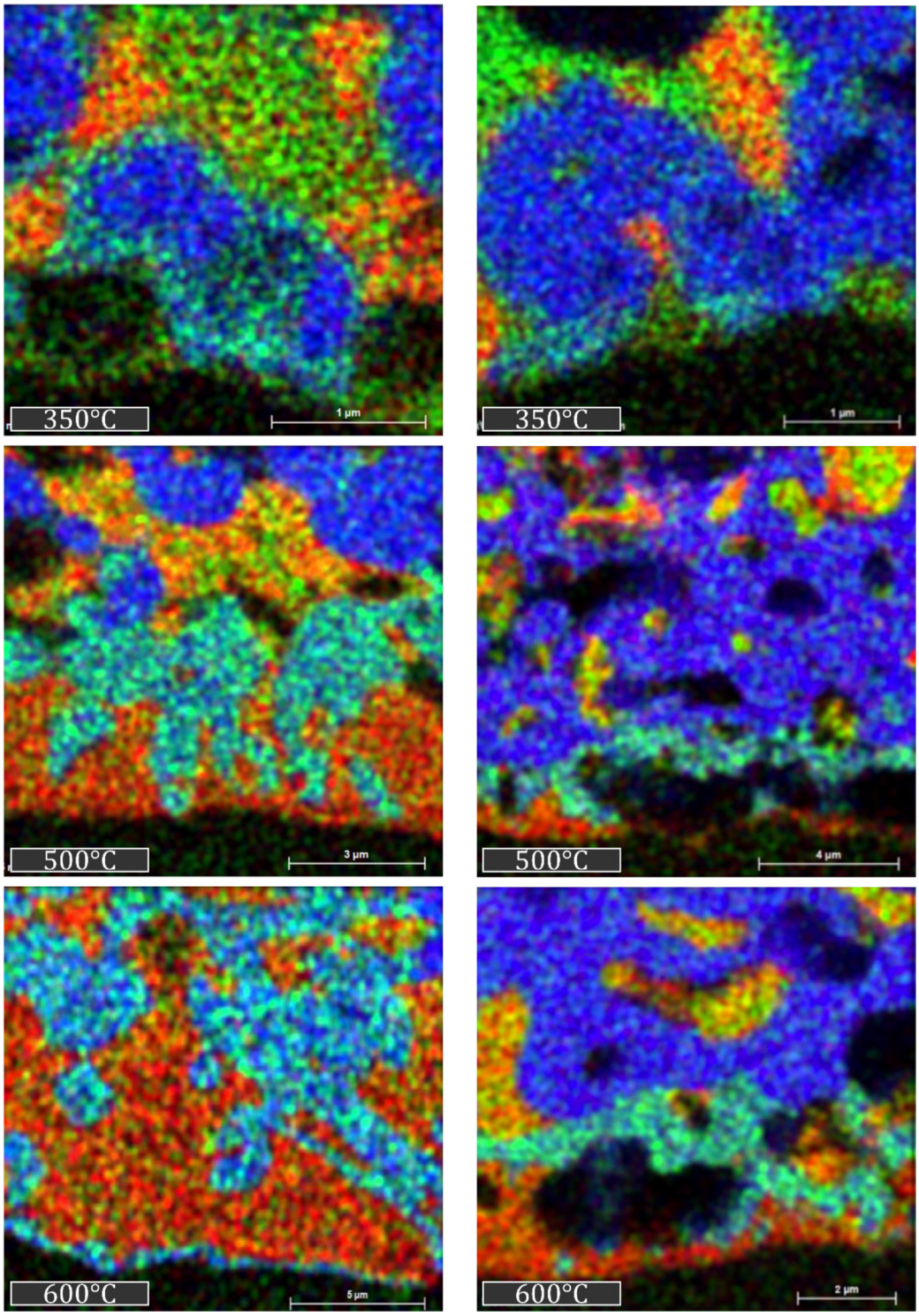

Fig. 5. EDX cross section maps of pastes on non-coated silicon for different RTP firing peak temperatures on the left side for an Ag:MO ratio of 50%:50% and on the right side of 75%:25%. Dark blue depicts here the silver intensity, green tellurium and red bismuth. A co-mapping is clearly visible for higher temperatures indicated by the color mix. Also, the movement of Te upwards and Bi downwards is visible.

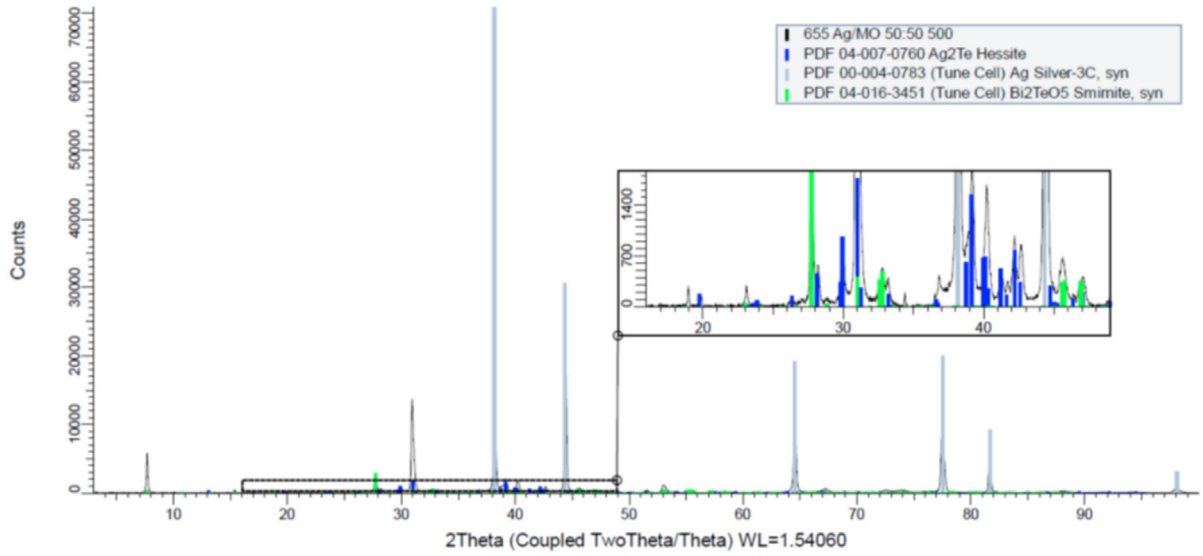

Fig. 6. XRD measurement of the RTP firing sample (peak temperature 500 °C) with an Ag:MO ratio of 50%:50%. The counts are shown depending on the 2θ angle, with a zoom on the area of interest. With dark blue, the peaks corresponding to Ag_2Te in hessite structure, in grey silver and in green the Bi_2TeO_5 are identified.

firing peak temperatures have been applied. Here, dark blue depicts the silver intensity, green tellurium and red bismuth. A co-mapping is clearly visible for increasing temperatures indicated by the color mix. Starting at low temperatures, Ag and Te show interaction at the interface and move upwards through the glassy layer. With higher temperatures, the glassy layer becomes increasingly Bi-rich, whereas Ag and Te show increased interaction up to a complete co-existence which is likely to be an alloying. For the higher Ag concentration on the right side, it is additionally visible that the Ag and Te movement upwards is reduced maybe due to less Te compared to the left side.

Figure 6 shows a corresponding XRD spectrum. The respective phases of the sample which was screen-printed with the paste consisting of Ag:MO ratio 50%:50% and RTP fired at 500 °C can be identified at the different peaks. Peaks associated with silver are indicated by gray lines. In green the mixed glass Bi_2TeO_5 can be identified and in dark blue the present mixture of Ag and Te as Ag_2Te in the hessite phase [35]. The latter proves above all the compound formation between Ag and Te, very likely by alloying.

3.3 Contact points

A major issue since the first publications in the field of Ag metallization of Si is that of contact points [36]. While a classical contacting is based on a direct connection of a silver crystallite in the silicon with the Ag paste bulk or the contact between silicon and Ag paste bulk [10,35], there are many considerations for indirect contacting paths. For this purpose, it must be ensured that there is either a conductive connection between individual silver crystallites or that metallic nanoparticles are present in the glass layer separated from each other within tunneling range of charge carriers.

For the full paste on a passivated and pyramidally textured wafer with n^+ emitter of 95 Ω/sq, an example of direct contacting can be seen in Figure 7. An EDX cross section of a Si pyramid is shown where a single Ag crystallite has grown into the Si bulk. We see that SiN_x:H is removed in the vicinity of this contact point, which suggests the etching of the passivation layer prior to Ag crystal growth. The constituents of the glassy paste components can be found moving towards the troughs between pyramids during firing, as described before.

The glass, identifiable mainly by the high oxygen concentration, also shows a corresponding proportion of Bi. Here, Te is also present in the glass but accumulates more strongly in some places.

In contrast, Figure 8 shows an example of a non-contact indirect path. Again, the movement of Bi to the pyramid trough and to the wafer surface is shown. The upward movement of Te, as well as the alloying of Te with Ag, is also visible. Here, within the glass layer, some thicker and thinner Ag spots can be seen, which seem to intersperse the entire glass. This effect seems more pronounced for increased Te contents in the glass, e.g. in Figure 8.

In addition, Ag_2Te, which is significantly lower in conductivity ($2.75 \cdot 10^{-3}$ Ωcm) [37] than pure silver ($1.59 \cdot 10^{-6}$ Ωcm), could still contribute in part to indirect silver contact. Figure 9 shows an EDX map of a region where the Ag crystallites formed on the Si surface are connected to the Ag paste bulk via an Ag_2Te phase. Bi-containing glass forms around the Te, but is also

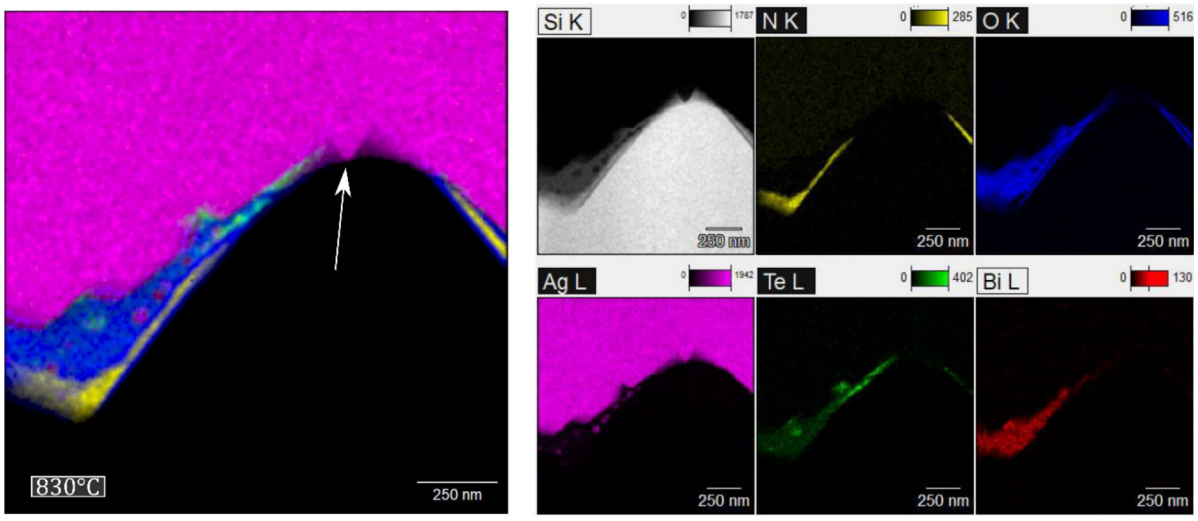

Fig. 7. EDX mapping for a cross section of a Si pyramid with Ag crystallite at the top, combined on the left, for each element respectively on the right. This is an example of a direct contact.

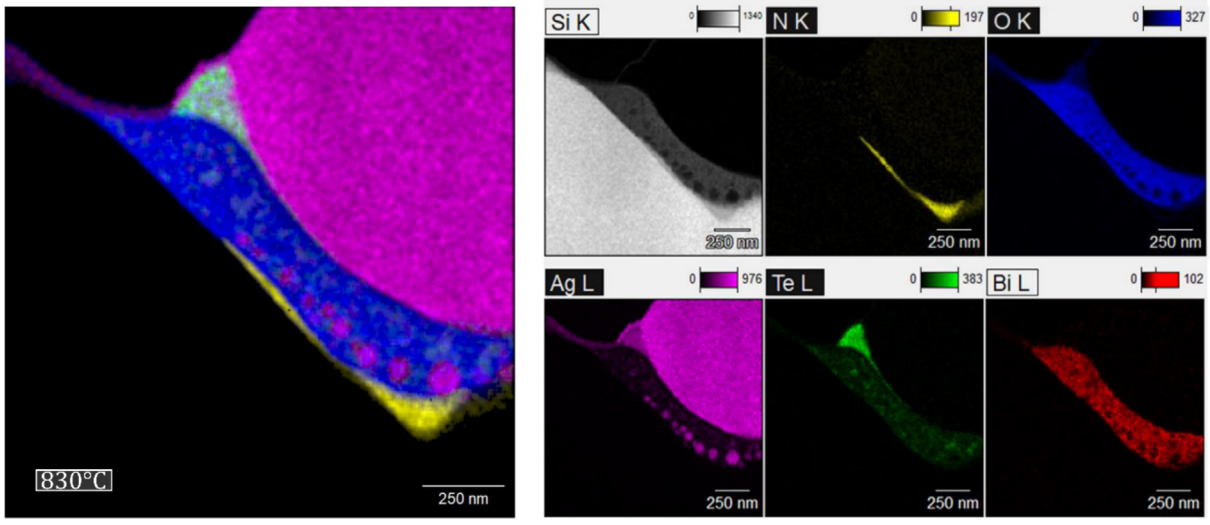

Fig. 8. EDX mapped cross section of a Si pyramid trough with Ag crystallite at the top, combined on the left, for each element respectively on the right. The Ag interspersed glass layer shows an example of a possible indirect contact via tunneling.

measured here in the region of the Ag_2Te. Indirect contact seems to be enabled by the Ag or Ag_2Te nanoparticles and by the Ag_2Te areas, respectively.

In addition to the previous findings, it is now observed that for the pyramidal structure, the etching of SiN_x:H does stop at the trough. This can be explained by the movement of the Te, which has already moved upward, so that the glass, now depleted of Te, cannot etch the SiN_x:H fast enough. The increase in silica content within the glassy phase is also believed to reduce the reactivity of the glassy phase. This proves at a fundamental level why contact formation in Te-based Ag pastes has a clear tendency to form contacts and crystallites at pyramid tips. Pyramid tips on which the passivation layer was preferentially etched during the firing process, additionally supported by Te moving upward, can be etched faster and stronger by Te and by Ag ions.

3.4 Contact model

Finally, the contact formation model is shown in Figure 10. A short conclusive overview, derived from the previous discussion is given in the following.

(A): First, the Ag paste consisting of Ag powder and crystalline mixed oxides is screen-printed on a SiN_x:H passivated n^+-emitter.

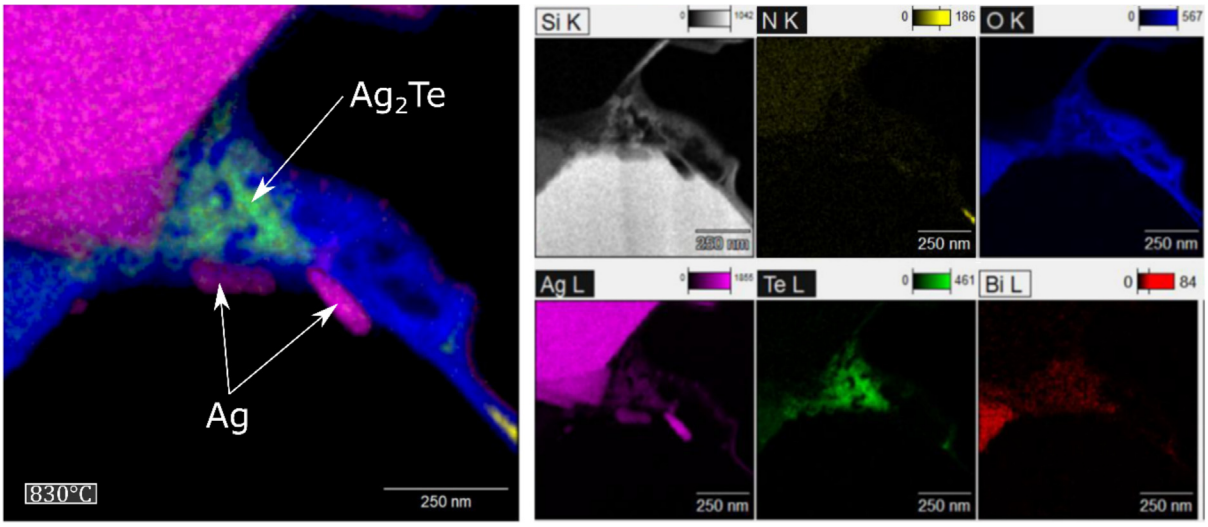

Fig. 9. EDX mapped cross section of a Si pyramid trough with Ag crystallite at the top, combined on the left, for each element respectively on the right. The Ag_2Te between the Ag bulk and the crystallites on the Si surface suggests an example of a possible indirect contact path.

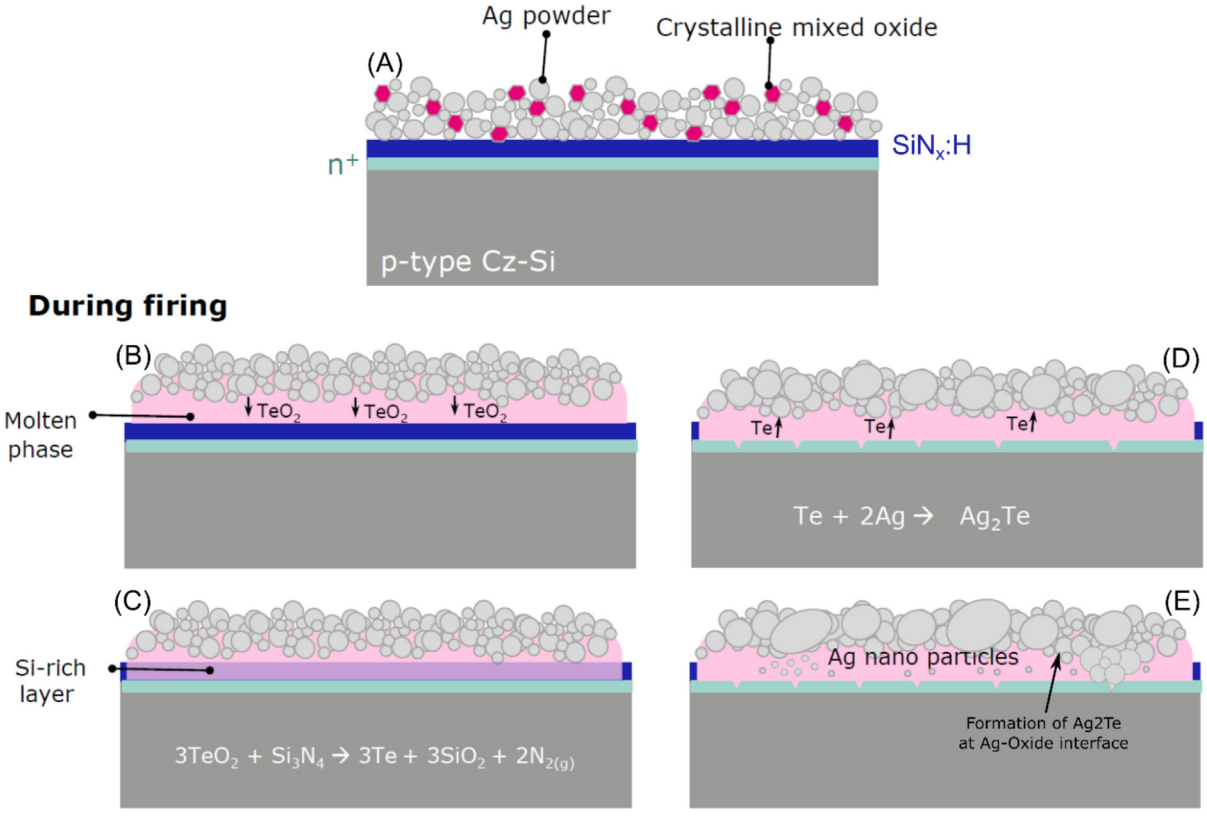

Fig. 10. Schematic model of contact formation with a PbO-free paste based on TeO_2 on an n^+-doped Si substrate. For detailed description, see text in Section 3.4.

(B): Observed from 300 °C: During firing, the paste reaches a partly molten state where the mixed crystalline oxides including TeO_2 move to the interface with the passivation layer and start etching this layer.

(C): Observed from 400 °C: The Bi_2TeO_5 and the TeO_2, which are partly responsible for the etching process of SiN_x:H and play a key role in etching the silicon, form atomic Te according to the redox reaction equations:

$$3TeO_2 + Si_3N_4 \rightarrow 3Te + 3SiO_2 + 2N_{2(g)},$$

$$TeO_2 + Si \rightarrow Te + SiO_2,$$

$$Bi_2TeO_5 + Si \rightarrow Te + SiO_2 + Bi_2O_3.$$

The SiN_x:H is here denoted as a stochiometric version in order to give a suggestion for reaction equations. The whole of the glassy layer becomes silica rich as the SiN_x:H and Si wafer is etched by the metal oxides.

(D): Simultaneously observed from 400 °C: While Ag adheres to the Si, the Te moves away from the interface and forms a compound of Ag_2Te, most likely also in an alloying process.

(E): In the final state, Ag and Ag_2Te nanoparticles are incorporated into the glass structure at the interface and may contribute to the current flow via tunneling or when connected to the Ag paste bulk.

4 Conclusion

In summary, Te seems to play a key role in the contacting of crystalline Si by Pb-free, Te-containing Ag pastes. It was observed that Ag can react with Te at the wafer surface due to the presence of Si and the redox reaction taking place. Using the paste system of crystalline metal compounds without glass frits, the motion and reaction of Ag with Te and Bi could be shown using EDX maps by increasing the oxide components. In addition, it was shown that the paste used with crystalline metal oxides behaves very comparable to the glass frit system above a certain firing peak temperature and can also keep up with the glass frit pastes on solar cell level concerning contact resistivity and efficiency. Contact resistances below 1 $m\Omega cm^2$ were measured for contacting both n^+ and p^+ polarities. Finally, an overview and model of contact formation with the present paste was presented.

The authors also like to thank Bärbel Rettenmaier and Walter Franchini for technical support during this work as well as Daniel Wurmbrand and Axel Herguth for the fruitful discussions on crystallography. Part of this work was supported by the German BMWi under contract no. 0324226A, Innovate UK and the Solar ERANet Co fund 045. The content is the responsibility of the authors.

Author contribution statement

Fabian Geml: Writing – review & editing, Writing – original draft, Methodology, Investigation, Formal analysis, Conceptualization. Benjamin Gapp: Investigation, Methodology, Formal analysis, Writing – original draft. Simon Johnson: Investigation, Methodology, Formal analysis. Patricia Sutton: Investigation, Methodology, Formal analysis, Writing – original draft, Writing – review & editing. Angela Goode: Investigation, Methodology. Jonathan Booth: Writing – review & editing, Supervision, Resources, Project administration, Funding acquisition. Heiko Plagwitz: Writing – review & editing, Validation, Supervision. Giso Hahn: Writing – review & editing, Supervision, Resources, Project administration, Funding acquisition.

References

1. A. Harter, J.I. Polzin, L. Tutsch, J. Temmler, M. Hofmann, A. Moldovan, F. Feldmann, IEEE J. Photovolt. **11**, 936 (2021)
2. C. Ballif, D.M. Huljić, G. Willeke, A. Hessler-Wyser, Appl. Phys. Lett. **82**, 1878 (2003)
3. B. Min, N. Wehmeier, T. Brendemuehl, A. Merkle, F. Haase, Y. Larionova, L. David, H. Schulte-Huxel, R. Peibst, R. Brendel, Sol. RRL **4**, 2000435 (2020)
4. E. Cabrera, S. Olibet, D. Rudolph, P.E. Vullum, R. Kopecek, D. Reinke, C. Herzog, D. Schwaderer, G. Schubert, Progr. Photovolt.: Res. Appl. **23**, 367 (2015)
5. International Roadmap for Photovoltaics (ITRPV), twelfth ed. (2021), pp. 1–83
6. T. Dullweber, M. Stöhr, C. Kruse, F. Haase, M. Rudolph, B. Beier, P. Jäger, V. Mertens, R. Peibst, R. Brendel, Sol. Energy Mater. Sol. Cells **212**, 110586 (2020)
7. D. Herrmann, A. Fell, S. Lohmueller, G. Mikolasch, C. Schmiga, A. Wolf, S.W. Glunz, Sol. Energy Mater. Sol. Cells **230**, 111182 (2021)
8. R. Hoenig, M. Duerrschnabel, W. van Mierlo, Z. Aabdin, J. Bernhard, J. Biskupek, O. Eibl, U. Kaiser, J. Wilde, F. Clement, D. Biro, Energy Procedia **43**, 27 (2013)
9. S. Tepner, L. Ney, M. Linse, A. Lorenz, M. Pospischil, F. Clement, IEEE J. Photovolt. **10**, 319 (2020)
10. S. Fritz, S. Riegel, S. Gloger, D. Kohler, M. König, M. Hörtheis, G. Hahn, Energy Procedia **38**, 720 (2013)
11. S. Fritz, M. König, S. Riegel, A. Herguth, M. Hörteis, G. Hahn, IEEE J. Photovolt. **5**, 145 (2015)
12. R. Lago, L. Pérez, H. Kerp, I. Freire, I. Hoces, N. Azkona, F. Recart, J.C. Jimeno, Progr. Photovolt. : Res. Appl. **18**, 20 (2010)
13. A. Frey, J. Engelhardt, S. Fritz, S. Gloger, G. Hahn, B. Terheiden, in *Proc. 29th European Photovoltaic Solar Energy Conference and Exhibition* (2014), pp. 656–660
14. S. Kontermann, M. Hörteis, M. Kasemann, A. Grohe, R. Preu, E. Pink, T. Trupke, Sol. Energy Mater. Sol. Cells **93**, 1630 (2009)
15. M.I. Jeong, S.E. Park, D.H. Kim, J.S. Lee, Y.C. Park, K.S. Ahn, C.J. Choi, J. Electrochem. Soc. **157**, H934 (2010)
16. S. Mack, D. Herrmann, M. Lenes, M. Renes, A. Wolf, Sol. RRL **5**, 2100152 (2021)
17. Y. Tachibana, A. Matsuda, M. Yoshimoto, Jpn. J. Appl. Phys. **59**, 090908 (2020)
18. D. Kim, S. Hwang, H. Kim, J. Korean Phys. Soc. **55**, 1046 (2009)
19. S.B. Cho, K.K. Hong, J.Y. Huh, H.J. Park, J.W. Jeong, Curr. Appl. Phys. **10**, S222 (2010)
20. Y. Zhang, Y. Yang, J. Zheng, W. Hua, G. Chen, Mater. Chem. Phys. **114**, 319 (2009)
21. K.K. Hong, S.B. Cho, J.Y. Huh, H.J. Park, J.W. Jeong, Metals Mater. Int. **15**, 307 (2009)

22. H.S. Kim, S.B. Cho, H. Kim, D. Kim, M. Dovrat, G. Eytan, J.Y. Huh, Progr. Photovolt.: Res. Appl. **24**, 1237 (2016)
23. J.D. Fields, M. Ahmad, V.L. Pool, J. Yu, D.G. Van Campen, P.A. Parilla, M.F. Toney, M.F.A.M. Van Hest, Nat. Commun. **7**, 11143 (2016)
24. M. Hörteis, T. Gutberlet, A. Reller, S.W. Glunz, Adv. Funct. Mater. **20**, 476 (2010)
25. G. Schubert, B. Fischer, P. Fath, in *Proceedings of photovoltaics PV in Europe Conference, Rome* (2002), pp. 343–346
26. D. Choi, H. Park, S. Bae, S.H. Shin, H. Han, B. Klöter, D. Kim, H.S. Lee, Y. Kang, Sol. Energy Mater. Sol. Cells **239**, 111587 (2022)
27. S.J. Jeon, S.M. Koo, S.A. Hwang, Sol. Energy Mater. Sol. Cells **93**, 1103 (2009)
28. S. Ueda, T. Kumagai, K. Yamaguchi, Mater. Trans. **46**, 1861 (2005)
29. K.K. Hong, S.B. Cho, J.S. You, J.W. Jeong, S.M. Bea, J.Y. Huh, Sol. Energy Mater. Sol. Cells **93**, 898 (2009)
30. S. Ueda, T. Kumagai, K. Yamaguchi, Mater. Trans. **48**, 1458 (2007)
31. ITRPV, International Technology Roadmap for Photovoltaics (ITRPV): Results 2021, VDMA e. V., Frankfurt (2022)
32. F. Geml, B. Gapp, M. Mehler, C. Ebert, J. Booth, P. Sutton, S. Johnson, B. Cela, H. Plagwitz, G. Hahn, in *Proc. 38th European Photovoltaic Solar Energy Conference and Exhibition* (2021), pp. 317–320
33. D. Mercurio, M. El Farissi, B. Frit, P. Goursat, Mater. Chem. Phys. **9**, 467 (1983)
34. O.K. Kang Min, N.S.P. Bhuvanesh, P. Shiv Halasyamani, Inorg. Chem. **40**, 1978 (2001)
35. J. Schneider, H. Schulz, Zeitsch. Kristallogr. **203**, 1 (1993)
36. G. Schubert, F. Huster, P. Fath, Sol. Energy Mater. Sol. Cells **90**, 3399 (2006)
37. M. Fujikane, K. Kurosaki, H. Muta, S. Yamanaka, J. Alloys. Compd. **387**, 4 (2005)

Cite this article as: Fabian Geml, Benjamin Gapp, Simon Johnson, Patricia Sutton, Angela Goode, Jonathan Booth, Heiko Plagwitz, Giso Hahn, Model for contact formation of novel TeO_2 containing Pb-free silver paste on n^+ and p^+ doped crystalline silicon, EPJ Photovoltaics. **14**, 8 (2023)